Joint Destriping and Segmentation of OCTA Images

Xiyin Wu[1,2,3], Dongxu Gao[3], Bryan M Williams[3], Amira Stylianides[4], Yalin Zheng[3,4], and Zhong Jin[1,2]

[1] School of Computer Science and Engineering, Nanjing University of Science and Technology, Nanjing 210094, China
zhongjin@njust.edu.cn, xiyinwu1990@gmail.com
[2] Key Laboratory of Intelligent Perception and System for High-Dimensional Information of Ministry of Education, Nanjing University of Science and Technology, Nanjing 210094, China
[3] Department of Eye and Vision Science, Institute of Ageing and Chronic Disease, University of Liverpool, Liverpool, L7 8TX, UK
yalin.zheng@liverpool.ac.uk
[4] St. Pauls Eye Unit, Royal Liverpool University Hospital, Liverpool, L7 8XP, UK

Abstract. As an innovative retinal imaging technology, optical coherence tomography angiography (OCTA) can resolve and provide important information of fine retinal vessels in a non-invasive and non-contact way. The effective analysis of retinal blood vessels is valuable for the investigation and diagnosis of vascular and vascular-related diseases, for which accurate segmentation is a vital first step. OCTA images are always affected by some stripe noises artifacts, which will impede correct segmentation and should be removed. To address this issue, we present a two-stage strategy for stripe noise removal by image decomposition and segmentation by an active contours approach. We then refine this into a new joint model, which improves the speed of the algorithm while retaining the quality of the segmentation and destriping. We present experimental results on both simulated and real retinal imaging data, demonstrating the effective performance of our new joint model for segmenting vessels from the OCTA images corrupted by stripe noise.

Keywords: Vessels segmentation · Destriping · OCTA.

1 Introduction

Retinal blood vessels health is integral to high quality human vision. Changes in the retinal vasculature have a close relationship with many ophthalmological and cardiovascular diseases, such as diabetic retinopathy (DR) and age-related macular degeneration (AMD) [13]. As an important computer-aided image analysis technique, retinal vessel segmentation is the first and most important step to detect the retinal vasculature. The segmentation of retinal vessels is a valuable precursor for further processing and analysis, such as retinal image registration,

feature extraction and localization of retinal structures, such as the fovea and optic disk [18].

To acquire imagery of fine retinal vessels, the commonly used techniques are fluorescein angiography (FA) and indocyanine green angiography (ICGA) [8]. Both FA and ICGA require intravenous dye injections, which can have adverse side effects and still only provide information relating to superficial blood vessels. Recently, an innovative technology called optical coherence tomography angiography (OCTA) has emerged as an effective way of visualizing the retinal vessels up to capillary level [14]. Retinal vessels at different depths of the retina revealed by OCTA are illustrated in Fig. 1. OCTA generates structural images of the retina based on laser light reflectance on the surface of moving red blood cells. Unlike FA and ICGA, OCTA is a non-invasive, fast, depth-resolved approach. OCTA can fully visualize choroidal neovascularization in AMD and small retinal neovascularization in DR, which are difficult to identify in FA. Therefore, the usage of OCTA in the diagnosis of vascular diseases is expected to increase significantly in the near future. Our work concerns the automated segmentation of retinal blood vessels in OCTA images.

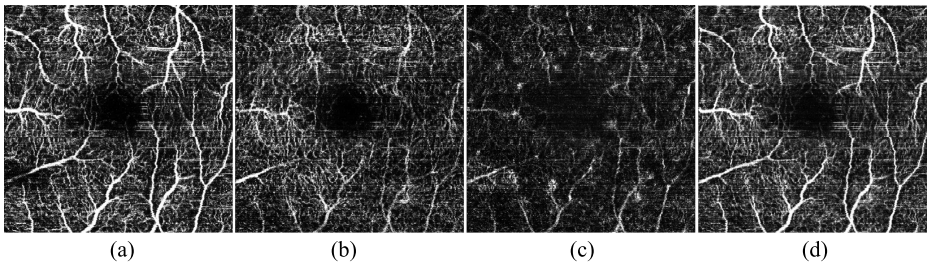

Fig. 1. OCTA images taken from different retinal layers. (a) Superficial vascular plexus (SVP): from internal limiting membrane to inner plexiform layer. (b) Deep vascular plexus (DVP): from inner plexiform layer to outer plexiform layer. (c) Avascular layer (AL): from outer plexiform layer to Bruch's membrane. (d) Whole retina (WR): from internal limiting membrane to Bruch's membrane.

As a relatively new modality, few studies exist and analyze the retinal vessels in OCTA and work in the OCTA vessel segmentation is still at an early stage in its development. Eladawi et al. [9] presented a joint Markov-Gibbs random field method to segment blood vessels from OCTA scans. The authors further estimated three local features from the segmented vessels to distinguish the status of DR patients [10]. Compared with OCTA, research in retinal vessel segmentation with color fundus images has a longer history. Many methods have been proposed over the last two decades, such as active contour models, wavelets methods, Gaussian mixture models, Adaboost and support vector machine, to name a few. One of the most commonly used segmentation approaches is active contours, such as the Chan-Vese model [5]. Chan-Vese model applied global statistics to the extraction of objects and was useful for objects with homogeneous intensity. To handle the non-uniform situation of the Chan-Vese model,

Sum et al. [15] developed a modified version by combining the local image contrast into a level set based active contour. Bashir et al. [1] grew a Ribbon of Twins active contour model to locate vessel edges under different conditions. Zhao et al. [17] segmented retinal vessels by developing an infinite perimeter active counter model with hybrid region information.

There are two limitations in the mentioned literatures in contributing to clinical diagnostics. Firstly, previous work on OCTA images have neglected the unavoidable noise problem. Additional image noise can arise from the OCTA image acquisition, eye motion and image pre-processing strategies. One of the most common types of noise is white horizontal stripe noise (see Fig. 1), which results from patient eye motion [12]. This problem has to be tackled before segmenting the retinal vessels to achieve effective, good-quality segmentation. Secondly, color fundus images can not provide depth information, limiting the analysis of choroidal neovascularization and small retinal neovascularization.

To overcome the above limitations, we first present a two-stage strategy for stripe noise removal and retinal vessel segmentation in OCTA images. This strategy removes stripe noise and Guassian noise from the image before segmenting the denoised image. Then we propose a joint model which achieves the two tasks simultaneously. Although there is no literature about removing stripe noise in OCTA images, remote sensing images suffer from similar noise and lots of related works have been explored. Image decomposition based methods have been considered for remote sensing image destriping in recent years and achieve good results [7]. Thus, image decomposition theory is chosen for the OCTA destriping problem. For vessel segmentation, a good choice is active contour models, which can not only provide smooth and closed contours but also achieve subpixel accuracy on vessel boundaries.

2 Methodology

2.1 Two-stage Strategy for Segmenting OCTA Images corrupted by Stripe Noise

A two-stage strategy is designed for segmenting OCTA images affected by stripe noise. In this strategy, we first remove the stripe noise and subsequently segment the retinal vessels.

Stripe Noise Removal Considering the stripe acquired along with the image content, we proceed with an image decomposition strategy, i.e. the given noisy image is decomposed to the desired clean image, the stripe noise and Guassian white noise. The model of the observed image can be formulated as:

$$Y = I + S + N \tag{1}$$

where Y is the given noisy image; I denotes the desired clean image; S is the additive stripe component; and N represents the linear assumption error and

Gaussian white noise. Stripe noise removal aims to estimate both I and S simultaneously from Y.

As shown in Fig. 1, the stripe noise has a salient structural characteristic, showing only in the horizontal direction. This is characterized by small rank for both periodical and nonperiodical stripes based on the analysis of [7]. Thus, the low-rank constraint is used for the stripe component. For the clean image, the anisotropic total variation (TV) regularization is used to achieve sharper boundaries in the reconstructed image, which will be important for segmenting vessels accurately. The image decomposition model is given as follows:

$$\min_{I,S} \frac{1}{2}\|I + S - Y\|_F^2 + \tau\|I\|_{\mathrm{TV}} + \lambda \mathrm{rank}(S) \tag{2}$$

where $\|I\|_{\mathrm{TV}} = \int_\Omega |\nabla I| dx$, τ and λ are two positive regularization parameters balancing the three terms. Ω is an open set representing the image domain, and $\nabla = (\nabla_x; \nabla_y)$ is the horizontal and vertical derivative operators of I, respectively. Due to the non-convexity of the rank constraint, the nuclear norm is introduced to replace the low-rank constraint as its convex substituted function [11]. The nuclear norm based image decomposition model is given by

$$\min_{I,S} \frac{1}{2}\|I + S - Y\|_F^2 + \tau\|I\|_{\mathrm{TV}} + \lambda\|S\|_*. \tag{3}$$

Segmentation of Vessels from Stripe Denoised Images Active contour models have demonstrated excellent performance in dealing with challenging segmentation problems including vessel segmentation [17, 1]. The Global Minimization of the Active Contour/Snake model (GMAC) [3] is introduced here for vessel segmentation. This model provides a convex solution for the well-known Chan-Vese (CV) model [5] and incorporates information from an edge detector. The GMAC model can be formulated as the energy minimization problem below:

$$\begin{aligned} \min_{u,c_1,c_2} \int_\Omega g(x,y)|\nabla u(x,y)| dxdy + \beta \int_\Omega u(x,y)(I(x,y) - c_1)^2 dxdy \\ + \beta \int_\Omega (1 - u(x,y))(I(x,y) - c_2)^2 dxdy \end{aligned} \tag{4}$$

where u is a characteristic function of a closed set Ω_C, C represents the boundaries of Ω, c_1 and c_2 are the average of $I(x,y)$ inside and outside of the segmented region respectively, and β is a small, positive balancing parameter. The first term is the TV-norm of u with weighted edge indicator function $g(x,y)$.

Thus, the vessel segmentation from stripe removed images is achieved by solving the problem (3) to obtain the stripe removed and denoised image I, followed segmenting I by solving the problem (4). The solvers of these two problems will be described later.

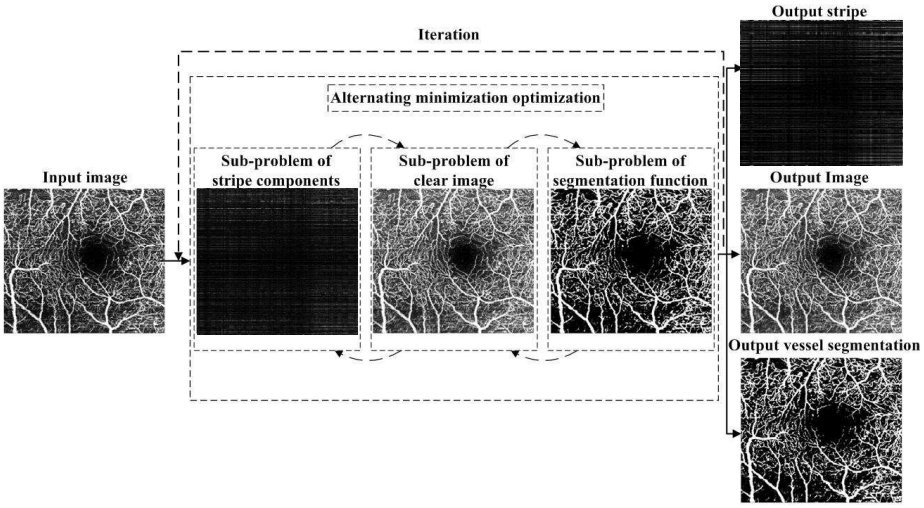

Fig. 2. Illustration of our joint model for segmentation images with stripe noise.

2.2 A New Joint Model for Segmenting Images Corrupted by Stripe Noise

In this section, we develop a joint model for simultaneously removing stripe noise and segmenting images. The model tackles the problems of image segmentation and considers the possible presence of stripe noise in a single model. The new joint model is formed by replacing the function I in the segmentation model (4) with the stripe-removed and denoised image term. Furthermore, the constraints of the decomposition problem (3) should be included in the joint model. The illustration of our proposed joint model is shown in Fig. 2. Building the constraints into the segmentation model, the new joint minimisation model is presented as follows:

$$\begin{aligned}\min_{I,S,u,c_1,c_2} \frac{1}{2}\|I+S-Y\|_F^2 + \tau\|I\|_{\mathrm{TV}} + \lambda\|S\|_* + \alpha\|u\|_{\mathrm{TV},g} + \frac{\beta}{2}u\|I-c_1\|_F^2 \\ + \frac{\beta}{2}(1-u)\|I-c_2\|_F^2\end{aligned} \tag{5}$$

where $\|\cdot\|_{\mathrm{TV},g}$ is the TV-norm with weighted function, α, β are small, positive balancing parameters. If α and β equal to 0, then the model (5) becomes the destriping model (3). The segmentation terms (fourth, fifth and sixth terms of (5)) obtain the intensity and spatial information from the stripe removed image I. To solve the joint model, each of the arguments is solved in turn. The detailed optimization process is presented as follows.

Stripe Component S Fixing other arguments, S is evaluated by minimising the following function:

$$\hat{S} = \arg\min_S \frac{1}{2}\|I+S-Y\|_F^2 + \lambda\|S\|_* \tag{6}$$

which can be solved by the following soft-thresholding operation:

$$\begin{cases} S^{k+1} = U(\text{shrink\_}L_*(\sum, \lambda))V^{\mathrm{T}} \\ \text{shrink\_}L_*(\sum, \lambda) = \text{diag}\{\max(\sum_{ii} - \lambda, 0)\}_i \end{cases} \tag{7}$$

where $Y - I = U \sum V^{\mathrm{T}}$ is the singular value decomposition of $Y - I^k$, and $\sum_{ii}$ is the diagonal element of the singular value matrix $\sum$.

Clean Image I Keeping other arguments fixed and minimising with respect to I, we have

$$\hat{I} = \arg\min_I \frac{1}{2}\|I + S - Y\|_F^2 + \tau\|I\|_{\mathrm{TV}} + \frac{\beta}{2}u\|I - c_1\|_F^2 + \frac{\beta}{2}(1-u)\|I - c_2\|_F^2 \tag{8}$$

where $\|I\|_{\mathrm{TV}}$ can be decomposed along the directions x and y:

$$\|I\|_{\mathrm{TV}} = \tau_x\|\nabla_x I\|_1 + \tau_y\|\nabla_y I\|_1 \tag{9}$$

where $\|\cdot\|_1$ represents the sum of absolute value of matrix elements. The weight τ along directions x and y is different due to the directional characteristics of the stripe component. The alternative direction multiplier method (ADMM) is introduced to solve the problem (8) efficiently. We convert this problem into two sub-problems. Let $D_x = \nabla_x I$, $D_y = \nabla_y I$, $D = [D_x, D_y]^{\mathrm{T}}$, $\nabla = [\nabla_x, \nabla_y]^{\mathrm{T}}$, $\tau = [\tau_x, \tau_y]^{\mathrm{T}}$, (8) equals to the following problem:

$$\begin{aligned} \{\hat{I}, \hat{D}\} = &\arg\min_{I, D_x, D_y} \frac{1}{2}\|I + S - Y\|_F^2 + \tau\|D\|_1 + \frac{\beta}{2}u\|I - c_1\|_F^2 \\ &+ \frac{\beta}{2}(1-u)\|I - c_2\|_F^2 + \frac{\gamma}{2}\|D - \nabla I - \frac{J}{\gamma}\|_F^2. \end{aligned} \tag{10}$$

The I-related sub-problem is followed by

$$\begin{aligned} \hat{I} = &\arg\min_{I, D_x, D_y} \frac{1}{2}\|I + S - Y\|_F^2 + \frac{\beta}{2}u\|I - c_1\|_F^2 \\ &+ \frac{\beta}{2}(1-u)\|I - c_2\|_F^2 + \frac{\gamma}{2}\|D - \nabla I - \frac{J}{\gamma}\|_F^2. \end{aligned} \tag{11}$$

We can obtain a closed form of (11) via fast 2-D Fourier transform (FFT):

$$I^{k+1} = \mathcal{F}^{-1}\left(\frac{\mathcal{F}(Y - S^{k+1} + \beta u^k {c_1}^k + \beta(1-u^k){c_2}^k) + \nabla^{\mathrm{T}}(\gamma^k D^k - J^k)}{1 + \beta + \gamma^k(\mathcal{F}(\nabla))^2}\right) \tag{12}$$

The D-related sub-problem is followed by

$$\hat{D} = \arg\min_D \tau\|D\|_1 + \frac{\gamma}{2}\|D - \nabla I - \frac{J}{\gamma}\|_F^2 \tag{13}$$

which can be solved by a soft shrinkage operator

$$\begin{cases} D^{k+1} = \text{shrink\_}L_1(\nabla I^{k+1} + \frac{J^k}{\gamma^k}, \frac{\tau}{\gamma^k}) \\ \text{shrink\_}L_1(r, \xi) = \frac{r}{|r|} * \max(r - \xi, 0). \end{cases} \tag{14}$$

Region Average Intensity Values c_1, c_2 Keeping other arguments fixed and minimising with respected c_1 and c_2, respectively. We have the equations for c_1 and c_2

$$c_1 = \frac{\int_\Omega u(x,y)I(x,y)dxdy}{\int_\Omega u(x,y)dxdy}, c_2 = \frac{\int_\Omega (1-u(x,y))I(x,y)dxdy}{\int_\Omega (1-u(x,y))dxdy} \tag{15}$$

which can be evaluated directly by giving the average intensities inside and outside of the segmentation contour. c_1 and c_2 in GMAC can be solved in a same way.

Segmentation Indicator Function u Minimising model (5) with respecting to u and fixing the other arguments, we have

$$\hat{u} = \arg\min_u \alpha\|u\|_{\mathrm{TV},g} + \frac{\beta}{2}u\|I-c_1\|_F^2 + \frac{\beta}{2}(1-u)\|I-c_2\|_F^2. \tag{16}$$

A convex regularization variational model is used according to [2]:

$$\begin{aligned}\{\hat{u},\hat{v}\} =& \arg\min_{u,v} \alpha\|u\|_{\mathrm{TV},g} + \frac{1}{2\theta}\|u+v-I\|_F^2 \\ &+ \frac{\beta}{2}(I-v)\|I-c_1\|_F^2 + \frac{\beta}{2}(1-I+v)\|I-c_2\|_F^2\end{aligned} \tag{17}$$

where the parameter θ is small so that we can approximate $I = u + v$. The function u denotes the geometric information, while v represents the texture information in the clean image I. Problem (17) can be solved by minimizing u and v iteratively.

The u-related sub-problem is followed by

$$\hat{u} = \arg\min_u \alpha\|u\|_{\mathrm{TV},g} + \frac{1}{2\theta}\|u+v-I\|_F^2. \tag{18}$$

The solution of (18) can be achieved efficiently by a fast dual projection algorithm. The derived solution is:

$$u^{k+1} = v^k - \alpha\theta \mathrm{div} p^{k+1} \tag{19}$$

where p is given by a fixed point method as follows:

$$p^{k+1} = \frac{p^k + \delta t \nabla(\mathrm{div}(p^k) - v/(\alpha\theta))}{1 + \frac{\delta t}{g(x,y)}|\nabla(\mathrm{div}(p^k) - v/(\alpha\theta))|}. \tag{20}$$

where $\delta t \leq 1/8$ is the temporal step.

The v-related sub-problem is followed by

$$\hat{v} = \arg\min_v \frac{1}{2\theta}\|u+v-I\|_F^2 + \frac{\beta}{2}(I-v)\|I-c_1\|_F^2 + \frac{\beta}{2}(1-I+v)\|I-c_2\|_F^2. \tag{21}$$

The v-minimization can be achieved through the following update:

$$v^{k+1} = \min\{\max\{u(x,y) - \frac{\beta\theta}{2}[(I(x,y)-c_2)^2 - (I(x,y)-c_1)^2], 0\}, 1\}. \tag{22}$$

u in GMAC can be solved in a similar way. The overall algorithm is presented in Algorithm 1.

Algorithm 1 Segmenting Images Corrupted by Stripe Noises by the Joint Model

Require: Image Y with stripe noise, parameters $\tau, \lambda, \alpha, \beta, \gamma, \theta, \rho$.
Ensure: Clean image I, stripe component S and segmentation indicator funcion u.
Initialize: set $J^1 = 0, I^1 = Y, u^1 = 0, v^1 = 0$
for $k = 1 : N$ **do**
  Compute S^{k+1} by solving (7)
  Compute I^{k+1} by solving (12)
  Compute D^{k+1} by solving (14)
  Compute c_1^{k+1} and c_2^{k+1} by solving (15)
  Compute u^{k+1} by solving (19)
  Compute v^{k+1} by solving (22)
  Update Lagrangian multipliers $J^{k+1} = J^k + \gamma^k(\nabla I^{k+1} - S^{k+1})$
  Update penalization parameters $\gamma^{k+1} = \gamma^k \cdot \rho$
end for

3 Results and Discussion

The proposed algorithms are evaluated in two parts: the effectiveness of destriping and the effectiveness of segmentation. All experiments are run in MATLAB (R2018a) (Mathworks, MA) on a desktop with 8GB RAM, Intel (R) Core (TM) i5-7500 CPU @ 3.40GHz. We denote the models to be compared and tested as follows:

D1: The weighted median filter denoising method [4].

D2: The wavelet denoising method [6].

N1: The two-stage strategy presented in this paper by destriping model (3) followed by segmentation model (4).

N2: The proposed joint model (5) for destriping and segmentation simultaneously.

3.1 Effectiveness of Destriping

In the experiment of stripe noise removal, simulated data and real data are employed to compare the performance of our methods (N1 and N2) with two denoising methods (D1 and D2). Two evaluation metrics are utilized. i.e. the peak signal-to-noise ratio (PSNR) and the structural similarity (SSIM) [16]. The two metrics are calculated by using equations (23) and (24), respectively.

$$PSNR = 10 \cdot \log_{10}\left(\frac{MAX_I^2}{MSE}\right) \tag{23}$$

$$SSIM(x, y) = \frac{(2\mu_x\mu_y + c_1)(2\sigma_{xy} + c_2)}{(\mu_x^2 + \mu_y^2 + c_1)(\sigma_x^2 + \sigma_y^2 + c_2)} \tag{24}$$

where MAX_I is the maximum pixel value of the noise-free image and MSE is the mean squared error between noise-free image and noisy image. x and y are two windows of an image. $\mu_x, \mu_y, \sigma_x^2, \sigma_y^2$ are the average of x, y and the variance of x, y, respectively. σ_{xy} is the covariance of x and y. c_1, c_2 are two variables.

Simulated experiments In simulated experiments, stripe noise is added into an FA image. As shown in Fig. 3(b), the destriping results of four methods are shown in Fig. 3 (c)-(f). Both D1 and D2 fail to remove the stripe noise. The proposed N1 and N2 can remove the stripes and retain stripe-free areas well.

The highest PSNR and SSIM values in each intensity scenario of simulated experiments are marked in bold in Table 1. Five different levels of stripes are added to the original image to test the robustness of our methods. The intensity denotes the mean absolute value of the stripe lines. Our joint model N2 achieves the best performance according to Table 1. As the stripe level increase, the advantage of our methods N1 and N2 over other methods becomes clearer.

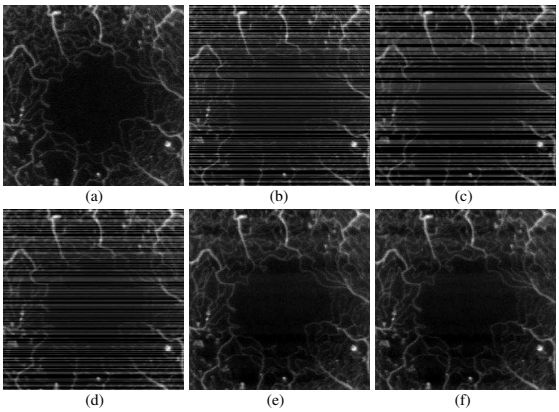

Fig. 3. Illustration of simulated destriping results. (a) Original image. (b) Image with added stripe noise. (c) Result of D1. (d) Result of D2. (e) Result of N1. (f) Result of N2.

Table 1. Quantitative results (PSNR (dB) and SSIM values) on simulated data.

Method	Stripe Noise									
	Intensity=10		Intensity=20		Intensity=30		Intensity=40		Intensity=50	
	PSNR	SSIM	PSNR	SSIM	PSNR	SSIM	PSNR	SSIM	PSNR	SSIM
Degraded	26.65	0.636	21.24	0.360	18.29	0.230	16.33	0.161	14.90	0.120
D1	26.78	0.624	21.27	0.377	18.15	0.254	16.09	0.187	14.60	0.147
D2	29.81	0.763	22.99	0.447	19.35	0.266	16.99	0.177	15.42	0.128
N1	34.99	0.945	33.81	**0.942**	31.31	0.923	28.61	**0.896**	26.03	0.858
N2	**35.00**	**0.947**	**33.82**	**0.942**	**31.94**	**0.928**	**28.66**	**0.896**	**26.11**	**0.859**

Real experiments The real OCTA stripe images are tested in this subsection. The proposed method is evaluated on 30 images collected from the Royal Liverpool University Hospital. Each image is taken in a 3mm*3mm field of view centered on the fovea from the internal limiting membrane (ILM) to the inner plexiform layer (IPL). We choose a representative image (see Fig. 4) and zoom in two regions of this image, i.e. R1 and R2. It is shown that our proposed method

N1 and N2 can remove most stripe noise, while D1 and D2 can just remove a little stripe noise.

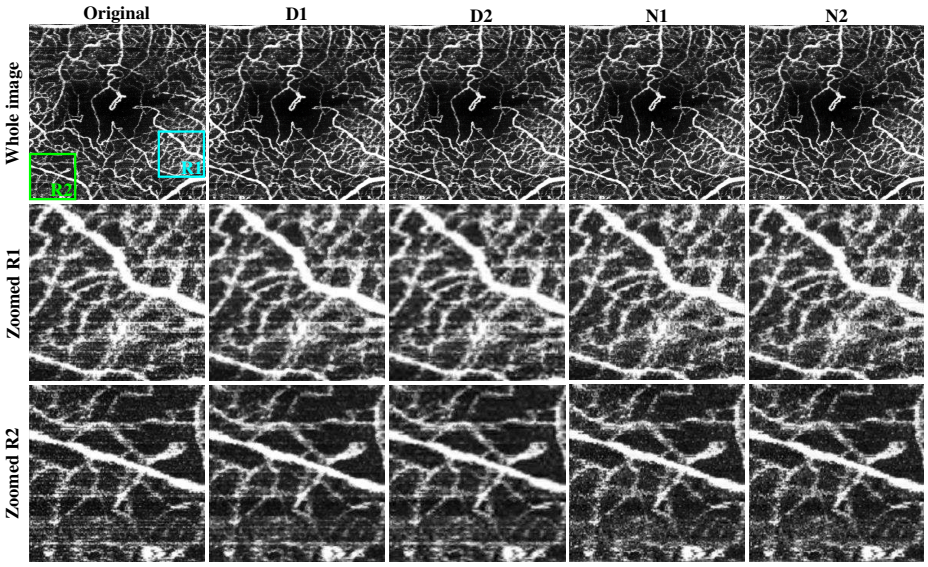

Fig. 4. Illustration of real OCTA destriping results. The first column shows the original OCTA image. The destriping results of D1, D2, N1 and N2 are shown from the second to fifth columns, respectively. The second and third rows show the zoomed regions R1 and R2 of the whole image, respectively.

3.2 Effectiveness of Segmentation

All images of the OCTA dataset mentioned in the real experiments (Section 3.1) are evaluated. The quantitative evaluation metric is accuracy, which is calculated as follows [17]:

$$Accuracy = \frac{TP + TN}{TP + FP + TN + FN} \tag{25}$$

where TP, FP, TN, FN indicate the true positive, false positive, true negative and false negative, respectively.

The computation of accuracy is based on the center line of the segmentation results and the center line annotation (see Fig. 5 (d)). The average accuracy values and CPU times of N1 and N2 are listed in Table 2. Compared to the two-stage strategy N1, our proposed joint model N2 can achieve higher accuracy in less time. We also give two segmentation examples in Fig. 5. N2 can generate competitive segmentation results to N1 efficiently.

4 Conclusion

This paper presented a two-stage strategy and proposed a new joint model for segmenting retinal blood vessels in OCTA images corrupted by stripe noise.

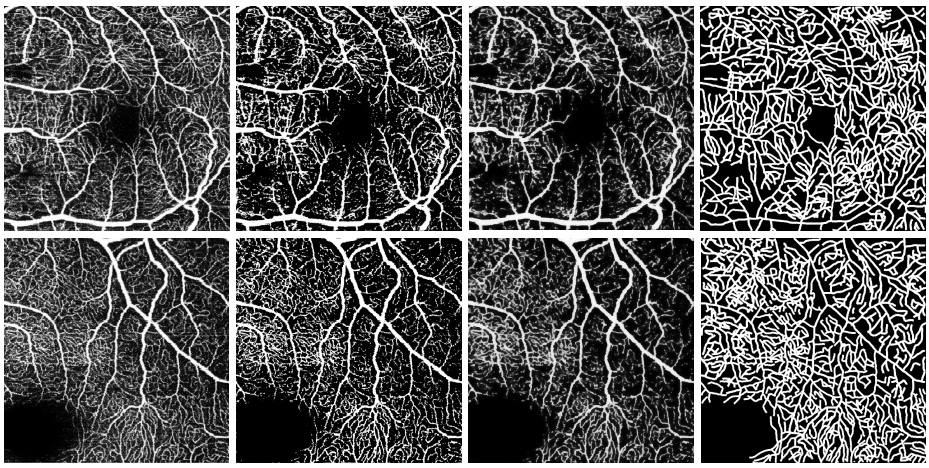

Fig. 5. Illustration of OCTA segmentation results. (a) Original image. (b) Segmentation result of N1. (c) Segmentation result of N2. (d) Center line annotation.

Table 2. Average accuracy values and cpu times of OCTA images segmentation.

Method	Accuracy	Times (s)
N1	0.9204	97.63
N2	0.9356	67.45

The two-stage strategy removed the stripe noise by a low-rank representation model, and then segmented the retinal blood vessels by an active contour model called GMAC. The joint model combined the models of stripe noise removal and vessel segmentation. These models solved the two problems efficiently, with the joint model solving the problems simultaneously, faster and more accurately. We tested the performance of our methods on an OCTA dataset from the Royal Liverpool University Hospital. The quantitative and efficiency comparison results showed that our proposed joint model provided excellent vessel segmentation results. It is believed that our work can inspire a way to consider the inclusion of stripe removal and clinical vessel analysis models.

Acknowledgments This work is partially supported by National Natural Science Foundation of China under Grant nos. 61872188, U1713208, 61602244, 61672287, 61702262, 61773215, and Postgraduate Research & Practice Innovation Program of Jiangsu Province under grant no. KYCX18_0426.

References

1. Al-Diri, B., Hunter, A., Steel, D.: An active contour model for segmenting and measuring retinal vessels. IEEE Transactions on Medical Imaging **28**(9), 1488–1497 (2009)

2. Aujol, J.F., Gilboa, G., Chan, T., Osher, S.: Structure-texture image decompositionmodeling, algorithms, and parameter selection. International Journal of Computer Vision **67**(1), 111–136 (2006)
3. Bresson, X., Esedolu, S., Vandergheynst, P., Thiran, J.P., Osher, S.: Fast global minimization of the active contour/snake model. Journal of Mathematical Imaging and Vision **28**(2), 151–167 (2007)
4. Brownrigg, D.: The weighted median filter. Communications of the ACM **27**(8), 807–818 (1984)
5. Chan, T.F., Vese, L.A.: Active contours without edges. IEEE Transactions on Image Processing **10**(2), 266–277 (2001)
6. Chang, S.G., Yu, B., Vetterli, M.: Adaptive wavelet thresholding for image denoising and compression. IEEE Transactions on Image Processing **9**(9), 1532–1546 (2000)
7. Chang, Y., Yan, L., Wu, T., Zhong, S.: Remote sensing image stripe noise removal: From image decomposition perspective. IEEE Transactions on Geoscience and Remote Sensing **54**(12), 7018–7031 (2016)
8. De Carlo, T.E., Romano, A., Waheed, N.K., Duker, J.S.: A review of optical coherence tomography angiography (octa). International Journal of Retina and Vitreous **1**(1), 5 (2015)
9. Eladawi, N., Elmogy, M., Helmy, O., Aboelfetouh, A., Riad, A., Sandhu, H., Schaal, S., El-Baz, A.: Automatic blood vessels segmentation based on different retinal maps from octa scans. Computers in Biology and Medicine **89**, 150–161 (2017)
10. Eladawi, N., Elmogy, M., Khalifa, F., Ghazal, M., Ghazi, N., Aboelfetouh, A., Riad, A., Sandhu, H., Schaal, S., El-Baz, A.: Early diabetic retinopathy diagnosis based on local retinal blood vessel analysis in optical coherence tomography angiography (octa) images. Medical Physics **45**(10), 4582–4599 (2018)
11. Fazel, M.: Matrix rank minimization with applications. Ph.D. thesis, PhD thesis, Stanford University (2002)
12. Moult, E., Choi, W., Waheed, N.K., Adhi, M., Lee, B., Lu, C.D., Jayaraman, V., Potsaid, B., Rosenfeld, P.J., Duker, J.S., et al.: Ultrahigh-speed swept-source oct angiography in exudative amd. Ophthalmic Surgery, Lasers and Imaging Retina **45**(6), 496–505 (2014)
13. Sheng, B., Li, P., Mo, S., Li, H., Hou, X., Wu, Q., Qin, J., Fang, R., Feng, D.D.: Retinal vessel segmentation using minimum spanning superpixel tree detector. IEEE Transactions on Cybernetics (99), 1–13 (2018)
14. Spaide, R.F., Fujimoto, J.G., Waheed, N.K., Sadda, S.R., Staurenghi, G.: Optical coherence tomography angiography. Progress in Retinal and Eye Research **64**, 1–55 (2018)
15. Sum, K., Cheung, P.Y.: Vessel extraction under non-uniform illumination: a level set approach. IEEE Transactions on Biomedical Engineering **55**(1), 358–360 (2008)
16. Wang, Z., Bovik, A.C., Sheikh, H.R., Simoncelli, E.P., et al.: Image quality assessment: from error visibility to structural similarity. IEEE Transactions on Image Processing **13**(4), 600–612 (2004)
17. Zhao, Y., Rada, L., Chen, K., Harding, S.P., Zheng, Y.: Automated vessel segmentation using infinite perimeter active contour model with hybrid region information with application to retinal images. IEEE Transactions on Medical Imaging **34**(9), 1797–1807 (2015)
18. Zhu, C., Zou, B., Zhao, R., Cui, J., Duan, X., Chen, Z., Liang, Y.: Retinal vessel segmentation in colour fundus images using extreme learning machine. Computerized Medical Imaging and Graphics **55**, 68–77 (2017)